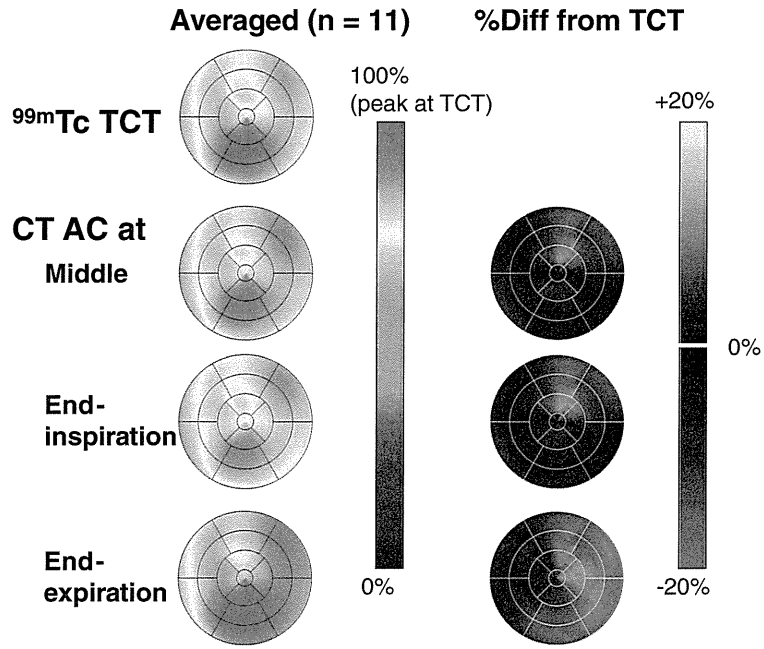

Figure 5 Polar maps of averaged radioactivity concentrations and percent differences from images corrected with TCT attenuation maps.

individual value was 9.3% ± 3.0% in the basal inferolateral segment for the EXP phase. It was considered that the relatively large differences in radioactivity concentrations of the EXP polar map, as shown in Figure 5, compared to the MID or the INS polar maps were due to the results over all subjects, but was not from outliers.

Discussion

This study investigated the effects of respiratory phases on breath-hold CT-based attenuation correction in cardiac SPECT with monitoring of the respiratory phase and amplitude. Reconstruction using CT attenuation maps at the INS and MID phases, with correction for attenuation and scatter, provided quantitative SPECT images that agreed with images derived from TCT-based attenuation maps. The SPECT images with CT attenuation maps at INS and MID phases showed similar radioactivity concentrations, as seen in Figures 4 and 5. This may be due to similarities between CT attenuation maps at INS and MID, for instance the separation between the surfaces of the inferior myocardial wall and the liver, as shown in Figure 3. Polar map analysis of the four attenuation maps showed no significant heterogeneity in any image dataset in terms of weight-normalized radioactivity concentrations.

The CT-AC images corrected with EXP attenuation maps differed significantly from the TCT-AC and CT-AC image datasets at INS and MID phases. In addition, for all segments, the percent differences from TCT-AC images indicated a bias of CT-AC images with EXP attenuation maps: a positive bias in anterior to anterolateral segments and a negative bias in inferior to inferoseptal segments for CT-AC images with both INS and MID attenuation maps, as shown in Figure 5. The magnitude of the bias for CT-AC images with EXP attenuation maps was larger than that of CT-AC images with the other respiratory attenuation maps. As previously reported, MBF was non-linearly related to the radioactivity concentration for ^{201}Tl kinetics [8,11]. Error with positive bias in the concentration propagated to error in MBF values more than negative bias with the same magnitude. Therefore, we considered the CT attenuation maps at the INS or MID phases to be preferable to those at the EXP phase. Instead of breath-hold CT acquisitions, respiratory gating in both SPECT and CT scans was expected to be another approach for CT-AC. Uniformity of radioactivity concentrations in myocardia has been improved by respiratory-gated SPECT acquisition [22]. Although respiration-related artifacts must be corrected ideally, the breath-hold CT-AC might be suitable for dynamic SPECT studies with low-dose injections, such as measurement of absolute MBF, which needed temporal changes in radioactivity concentrations.

Although no significant heterogeneity in regional radioactivity concentrations was observed, Figures 4 and 5 show reduced radioactivity concentrations in the anterior regions near the apexes and increased concentrations in the inferior regions in images with all attenuation maps. Potential reasons for the reduced concentrations are as follows: first, residual errors in

registration between an attenuation map and a SPECT image. Fricke et al. reported that a 3.5-mm misalignment in the ventrodorsal direction induced a spurious defect in the anteroseptal wall in a phantom study [23]. The second reason is spillover from the anterior wall due to partial volume effects. The anterior wall was surrounded by void space in terms of ^{201}Tl concentration. Spillover from the wall, particularly near the apex, could be affected by the partial volume effects three-dimensionally. In contrast, possible reasons for relatively high concentrations in the inferolateral to inferior wall are as follows: (1) residual errors in registration as seen with the anterior wall, (2) overestimation of attenuation effects around the inferolateral to lateral walls caused by the liver, as pointed out by Cook et al. [18], and (3) spillover from other organs. Little effect of overlap between the heart and the liver was reported by McQuaid and Hutton [24]. However, in their numerical phantom study, spatial resolution effects of a SPECT scanner were excluded, and the assumed activity ratio between the myocardium and the liver was 75:30. Their experimental conditions were different from those in our human study, specifically the spatial resolution of the SPECT scanner and the activity ratio of the two organs (liver/anterolateral myocardium = 1.1 ± 0.3, range = 0.7 to 1.7). High radioactivity concentration was also observed in the left kidney (the activity ratio of the left kidney/anterolateral myocardium = 1.5 ± 0.3, range = 1.1 to 2.0). It could cause additional spillover to the anterolateral myocardium. Anatomical information from the CT image prior to spatial resolution matching to SPECT was expected to help correct for the spillover and, thus, produce a more accurate quantitative SPECT image.

In this study, the use of CT-AC attenuation maps with breath holding was validated at resting conditions. In order to measure coronary flow reserve, a stress SPECT scan is needed. A series of resting and stress scans could take a relatively long time. For optimal comfort, the patient would step off the scanner bed during the interval between the two scans, or the two scans would be carried out on different days. In such cases, additional CT-AC scans would be needed for accurate attenuation correction. The respiration amplitude observed by the monitoring system was 8.50 ± 5.58 (2.51 to 17.50) mm. The accuracy of the system, 0.35-mm RMS, was considered sufficient to discriminate the three respiratory phases during a single session, that is, while a subject lay continuously on the scanner bed. However, it would be difficult, using the monitoring system, to ensure inter-subject reproducibility of the amplitude of respiratory motion as well as intra-subject results obtained during different sessions. The respiratory motion was estimated by measuring positions of the infrared-reflective target placed on the abdominal surface. The amplitudes and directions of surface movements depend on the individual subject, the location of the target, and any non-linear deformation of the abdominal surface and internal organs.

The registration of an attenuation map and a pre-reconstructed SPECT image, prior to reconstruction of a quantitative SPECT image corrected for attenuation and scatter, was limited to translations in three spatial directions. If a rigid-body model including rotations or a non-linear registration was employed, an image corrected with CT-AC at the EXP phase might provide a consistent result with a TCT-based scan or CT-AC at the other respiratory phases. However, the use of INS or MID attenuation maps has an advantage over the EXP attenuation map in terms of separation between the heart and the liver surfaces, which would contribute to accurate registration of attenuation maps and pre-reconstructed SPECT images. As shown in Table 1, translations toward caudal directions were needed to align CT attenuation maps at any respiration phases to SPECT images. The reason could be different baseline positions of the hearts during breath-hold CT acquisitions and SPECT acquisitions with breathing freely, as previously reported by Pan et al. [25]. For TCT attenuation map, no alignment between the attenuation map and SPECT image was needed essentially because temporal resolutions of TCT and SPECT scans for respiratory motions were nearly identical. The slight shifts of TCT attenuation maps to SPECT images in cephalad/caudal directions, 2.4 ± 2.1 mm, might be caused by global and/or intra-torso motions of subjects.

Conclusion

Use of breath-hold CT attenuation maps at end-inspiration and middle phases for attenuation and scatter corrections demonstrated accurate quantitative images in cardiac SPECT/CT studies. This technique might be applicable to routine clinical study. Quantitative assessment of absolute MBF and coronary flow reserve in clinical settings would be an additional potential application.

Competing interests

The authors declare that they have no competing interests.

Acknowledgments

This study was supported by a Grant for Translational Research from the Ministry of Health, Labour and Welfare of Japan, a Grant for Advanced Medical Technology from the Ministry of Health, Labour and Welfare of Japan, and, in part, a Grant-in-Aid for Scientific Research from the Ministry of Education, Culture, Sports, Science and Technology of Japan.

Authors' contributions

KaK participated in the development of a respiratory motion indicator system and analysis of SPECT data. KS participated in the image processing for reconstruction of SPECT images. YH participated in the measurement of respiratory motions. TM and TZ participated in the discussion of spillover effects and misregistration effects between emission and attenuation data

and helped to draft the manuscript. MF and YN carried out SPECT/CT studies as radiological technologists. KF and KeK participated as physicians. HI conceived the application of the breath-hold CT to the cardiac SPECT study and helped to draft the manuscript. All authors read and approved the final manuscript.

Author details
[1]Department of Investigative Radiology, National Cerebral and Cardiovascular Center Research Institute, 5-7-1 Fujishirodai, Suita, Osaka 565-8565, Japan. [2]Department of Radiology and Nuclear Medicine, National Cerebral and Cardiovascular Center Hospital, 5-7-1 Fujishirodai, Suita, Osaka 565-8565, Japan. [3]Graduate School of Medicine/Faculty of Medicine, Osaka University, 1-1 Yamadaoka, Suita, Osaka 565-0871, Japan.

Received: 19 March 2012 Accepted: 22 June 2012
Published: 22 June 2012

References

1. Hendel RC, Berman DS, Cullom SJ, Follansbee W, Heller GV, Kiat H, Groch MW, Mahmarian JJ: **Multicenter clinical trial to evaluate the efficacy of correction for photon attenuation and scatter in SPECT myocardial perfusion imaging.** *Circulation* 1999, **99**:2742–2749.
2. Bailey DL: **Transmission scanning in emission tomography.** *Eur J Nucl Med* 1998, **25**:774–787.
3. Bailey DL, Hutton BF, Walker PJ: **Improved SPECT using simultaneous emission and transmission tomography.** *J Nucl Med* 1987, **28**:844–851.
4. Bailey DL, Robinson M, Meikle SR, Bye PT: **Simultaneous emission and transmission measurements as an adjunct to dynamic planar gamma camera studies.** *Eur J Nucl Med* 1996, **23**:326–331.
5. Meikle SR, Hutton BF, Bailey DL: **A transmission-dependent method for scatter correction in SPECT.** *J Nucl Med* 1994, **35**:360–367.
6. Narita Y, Eberl S, Iida H, Hutton BF, Braun M, Nakamura T, Bautovich G: **Monte Carlo and experimental evaluation of accuracy and noise properties of two scatter correction methods for SPECT.** *Phys Med Biol* 1996, **41**:2481–2496.
7. Narita Y, Iida H, Eberl S, Nakamura T: **Monte Carlo evaluation of accuracy and noise properties of two scatter correction methods for ^{201}Tl cardiac SPECT.** *IEEE Trans Nucl Sci* 1997, **44**:2465–2472.
8. Iida H, Eberl S: **Quantitative assessment of regional myocardial blood flow with thallium-201 and SPECT.** *J Nucl Cardiol* 1998, **5**:313–331.
9. Iida H, Narita Y, Kado H, Kashikura A, Sugawara S, Shoji Y, Kinoshita T, Ogawa T, Eberl S: **Effects of scatter and attenuation correction on quantitative assessment of regional cerebral blood flow with SPECT.** *J Nucl Med* 1998, **39**:181–189.
10. Iida H, Shoji Y, Sugawara S, Kinoshita T, Tamura Y, Narita Y, Eberl S: **Design and experimental validation of a quantitative myocardial ^{201}Tl SPECT System.** *IEEE Trans Nucl Sci* 1999, **46**:720–726.
11. Iida H, Eberl S, Kim KM, Tamura Y, Ono Y, Nakazawa M, Sohlberg A, Zeniya T, Hayashi T, Watabe H: **Absolute quantitation of myocardial blood flow with (201)Tl and dynamic SPECT in canine: optimisation and validation of kinetic modelling.** *Eur J Nucl Med Mol Imaging* 2008, **35**:896–905.
12. Koepfli P, Hany TF, Wyss CA, Namdar M, Burger C, Konstantinidis AV, Berthold T, Von Schulthess GK, Kaufmann PA: **CT attenuation correction for myocardial perfusion quantification using a PET/CT hybrid scanner.** *J Nucl Med* 2004, **45**:537–542.
13. Willowson K, Bailey DL, Baldock C: **Quantitative SPECT reconstruction using CT-derived corrections.** *Phys Med Biol* 2008, **53**:3099–3112.
14. Bacharach SL: **PET/CT attenuation correction: breathing lessons.** *J Nucl Med* 2007, **48**:677–679.
15. Goetze S, Brown TL, Lavely WC, Zhang Z, Bengel FM: **Attenuation correction in myocardial perfusion SPECT/CT: effects of misregistration and value of reregistration.** *J Nucl Med* 2007, **48**:1090–1095.
16. Goetze S, Wahl RL: **Prevalence of misregistration between SPECT and CT for attenuation-corrected myocardial perfusion SPECT.** *J Nucl Cardiol* 2007, **14**:200–206.
17. Alessio AM, Kohlmyer S, Branch K, Chen G, Caldwell J, Kinahan P: **Cine CT for attenuation correction in cardiac PET/CT.** *J Nucl Med* 2007, **48**:794–801.
18. Cook RA, Carnes G, Lee TY, Wells RG: **Respiration-averaged CT for attenuation correction in canine cardiac PET/CT.** *J Nucl Med* 2007, **48**:811–818.
19. QSPECT Group Web Page: *QSPECT Group Web Page.*; . www.qspect.org.
20. Jia L, Tsui BMW, Welch A, Frey EC, Gullberg GT: **Energy window optimization in simultaneous technetium-99 m TCT and thallium-201 SPECT data acquisition.** *Nuclear Science, IEEE Transactions* 1995, **42**:1207–1213.
21. Cerqueira MD, Weissman NJ, Dilsizian V, Jacobs AK, Kaul S, Laskey WK, Pennell DJ, Rumberger JA, Ryan T, Verani MS: **Standardized myocardial segmentation and nomenclature for tomographic imaging of the heart: a statement for healthcare professionals from the Cardiac Imaging Committee of the Council on Clinical Cardiology of the American Heart Association.** *Circulation* 2002, **105**:539–542.
22. Kovalski G, Israel O, Keidar Z, Frenkel A, Sachs J, Azhari H: **Correction of heart motion due to respiration in clinical myocardial perfusion SPECT scans using respiratory gating.** *J Nucl Med* 2007, **48**:630–636.
23. Fricke H, Fricke E, Weise R, Kammeier A, Lindner O, Burchert W: **A method to remove artifacts in attenuation-corrected myocardial perfusion SPECT introduced by misalignment between emission scan and CT-derived attenuation maps.** *J Nucl Med* 2004, **45**:1619–1625.
24. McQuaid SJ, Hutton BF: **Sources of attenuation-correction artefacts in cardiac PET/CT and SPECT/CT.** *Eur J Nucl Med Mol Imaging* 2008, **35**:1117–1123.
25. Pan T, Mawlawi O, Nehmeh SA, Erdi YE, Luo D, Liu HH, Castillo R, Mohan R, Liao Z, Macapinlac HA: **Attenuation correction of PET images with respiration-averaged CT images in PET/CT.** *J Nucl Med* 2005, **46**:1481–1487.

doi:10.1186/2191-219X-2-33
Cite this article as: Koshino *et al.*: Breath-hold CT attenuation correction for quantitative cardiac SPECT. *EJNMMI Research* 2012 2:33.

IOP PUBLISHING PHYSICS IN MEDICINE AND BIOLOGY

Phys. Med. Biol. **57** (2012) 7481–7492 doi:10.1088/0031-9155/57/22/7481

Monte Carlo estimation of scatter effects on quantitative myocardial blood flow and perfusable tissue fraction using 3D-PET and ^{15}O-water

Yoshiyuki Hirano[1], Kazuhiro Koshino[1], Hiroshi Watabe[2], Kazuhito Fukushima[3] and Hidehiro Iida[1]

[1] Department of Bio-medical Imaging, National Cerebral and Cardiovascular Center Research Institute, 5-7-1 Fujishiro-dai, Suita City, Osaka, 565-8565 Japan
[2] Department of Molecular Imaging in Medicine, Osaka University Graduate School of Medicine, Yamada Oka 2-2, Suita City, Osaka 565-0871 Japan
[3] Department of Radiology, National Cerebral and Cardiovascular Center, 5-7-1 Fujishiro-dai, Suita City, Osaka, 565-8565 Japan

E-mail: yhirano@nirs.go.jp

Received 28 March 2012, in final form 13 September 2012
Published 26 October 2012
Online at stacks.iop.org/PMB/57/7481

Abstract

In clinical cardiac positron emission tomography using ^{15}O-water, significant tracer accumulation is observed not only in the heart but also in the liver and lung, which are partially outside the field-of-view. In this work, we investigated the effects of scatter on quantitative myocardium blood flow (MBF) and perfusable tissue fraction (PTF) by a precise Monte Carlo simulation (Geant4) and a numerical human model. We assigned activities to the heart, liver, and lung of the human model with varying ratios of organ activities according to an experimental time activity curve and created dynamic sinograms. The sinogram data were reconstructed by filtered backprojection. By comparing a scatter-corrected image (SC) with a true image (TRUE), we evaluated the accuracy of the scatter correction. TRUE was reconstructed using a scatter-eliminated sinogram, which can be obtained only in simulations. A scatter-uncorrected image (W/O SC) and an attenuation-uncorrected image (W/O AC) were also constructed. Finally, we calculated MBF and PTF with a single tissue-compartment model for four types of images. As a result, scatter was corrected accurately, and MBFs derived from all types of images were consistent with the MBF obtained from TRUE. Meanwhile, the PTF of only the SC was in agreement with the PTF of TRUE. From the simulation results, we concluded that quantitative MBF is less affected by scatter and absorption in 3D-PET using ^{15}O-water. However, scatter correction is essential for accurate PTF.

(Some figures may appear in colour only in the online journal)

0031-9155/12/227481+12$33.00 Printed in the UK & the USA 7481

1. Introduction

Recent models of commercial positron emission tomography (PET) or PET-computed tomography (PET-CT) systems provide a three-dimensional (3D) (without septa) acquisition mode that allows injection of a lower activity of tracers compared with the two-dimensional (2D) (septa-extended) mode, because of increased sensitivity of the systems. However, scatter fraction, number of random events, and counting losses are higher than those observed in the 2D acquisition mode, suggesting the need for accurate correction methods, including correction of scatter originating from activity outside the field-of-view (FOV).

The benefit of the 3D mode has been demonstrated in brain imaging (Cherry *et al* 1993, Sadato *et al* 1997, Moreno-Cantu *et al* 1998, Ibaraki *et al* 2008) and the mode is widely accepted in whole-body PET oncology imaging (Lodge *et al* 2006), but is not in widespread use in cardiac studies (deKemp *et al* 2007, Brink *et al* 1991). Some direct comparisons between 2D and 3D in quantitative cardiac studies have been reported for ^{18}F-FDG (Lubberink *et al* 2004), ^{13}N-ammonia (Roelants *et al* 2006, Schepis *et al* 2007), ^{15}O-water (Schäfers *et al* 2002), and ^{82}Ru (Votaw and White 2001, Knesaurek *et al* 2003). All the studies obtained positive results except for that of Votaw and White, which demonstrated disadvantages of the 3D mode due to increased scatter and random events.

^{15}O-water is an ideal tracer because it diffuses immediately and produces no metabolites in tissues. As such it is considered to be the gold standard for noninvasive quantification of myocardial blood flow (MBF) (Knuuti *et al* 2009, Knaapen *et al* 2010). In addition, due to its short half-life (122.24 s), both rest and stress assessments are feasible within a short time period. The quantitative accuracy of absolute MBF measurements in 3D-PET has been compared between 2D and 3D in dogs (Roelants *et al* 2006), and between 3D and a microsphere in pigs (Schäfers *et al* 2002). However, the amount of scatter depends on the distribution of activity and absorbers in the entire body, and therefore different results would be obtained in humans than those derived thus far in animal studies.

The aim of this study was to use a precise simulation of 3D-PET and ^{15}O-water to clarify the impact of scatter on quantitative MBF and perfusable tissue fraction (PTF) measurements in humans. For this purpose, we used the Monte Carlo simulation library Geant4 (Agostinelli *et al* 2003) and a numerical human model. The simulation tool was also validated by comparing the scatter fraction and an annulus phantom image with experimental results prior to the cardiac PET simulation.

2. Materials and methods

2.1. Monte Carlo simulation

We used the Monte Carlo simulation library Geant4 (version 9.2) to trace annihilation gamma rays from their generation points to scintillation crystals. The geometrical configuration was constructed for the ECAT ACCEL (Siemens, Knoxville, TN, USA) PET scanner described in the following section. To enhance the realism of the simulation, we used a numerical human model with a configuration that included not only the scintillator ring but also scanner components such as photo multiplier tubes, front shield, septa, the bed for the patient, and the housing of the equipment, which slightly increased scatter (Hirano *et al* 2010). An illustration of the simulation setup is presented in figure 1.

2.2. PET system

The PET scanner reproduced in the cardiac 3D-PET simulation was the ECAT ACCEL. The scanner was also used for validation of the simulation. The scanner employed lutetium silicon

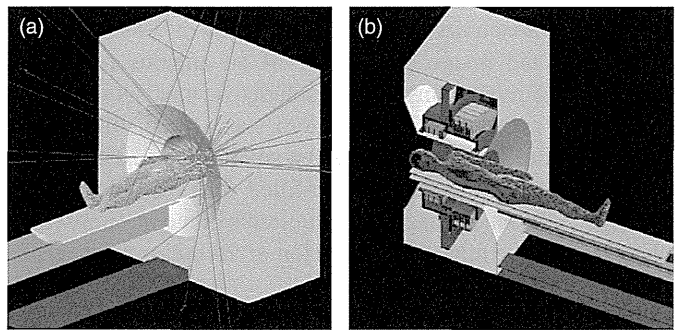

Figure 1. (a) Illustration of Geant4 simulation with a numerical human model. Radial lines drawn outward from the heart show gamma ray tracks. (b) Cross-sectional image through the center of the scanner. The PET configuration included the scintillator ring, photo multiplier tubes, front shield, septa, bed, and housing of equipment.

oxide scintillation crystals arranged in 24 detector rings covering a 16.4 cm axial FOV, 82.4 cm ring diameter, and 56.2 cm patient port, and it provided 47 sections with an interslice spacing of 3.375 mm. The crystals had dimensions of 6.45 mm $\times$ 6.45 mm $\times$ 25 mm (transaxial x axial x depth), and the crystal blocks were separated in an 8 $\times$ 8 array. The total number of detector blocks was 144, and thus one ring consisted of 384 elements. The scanner could be operated in both 2D and 3D modes. The radial and axial spatial resolutions were 6.22 and 5.71 mm full width at half maximum (FWHM), respectively, at a radial distance of 1 cm from the center. The energy window of the system was set to 350–650 keV. The scanner acquired direct and oblique sinograms with a maximum ring difference of 12 and a span of 3 in the 3D mode, and 175 3D sinograms (192 views, 192 bins) were created. The system performance has been previously described by Herzog *et al* (2004).

2.3. Numerical human model

A numerical human model was employed for the realistic simulation of the cardiac PET. The numerical model for a Japanese adult was developed by Nagaoka *et al* (2004) based on MRI images of the average Japanese body type, and used heights of 173.2 and 160.8 cm and weights of 65 and 53 kg for males and females, respectively. The model consisted of 320 $\times$ 160 $\times$ 866/804 voxels (for males and females, respectively) with a 2 mm cubic voxel, with the identification number for one of 51 organs or tissue types assigned to each voxel. In this study, we used the male model. The model was entered into Geant4 by implementing *G4PhantomParameterisation*, combining eight voxels into one to reduce computation time, and thus the simulation had a 4 mm spatial resolution for the numerical human model. We calculated the attenuation coefficients, which were not provided by the model, using the compositions and densities of soft tissue, skeleton, lung, adipose tissue, glandular tissue, bone, muscle, skin, brain, eye, thyroid, upper face, larynx, trachea, gastrointestinal tract, testis, urinary bladder, spleen, heart, pancreas, liver, kidney, breast, and blood available in Akkurt and Echerman (2007).We assigned density and composition data of the tissues listed above to the 51 organs and tissue types in the model.

2.4. Validation of the simulation

In order to validate the simulation, we compared the scatter fraction measured during the simulation with an experimental value that was measured according to the NEMA-NU 2007,

which considered the intrinsic radioactivity of ^{176}Lu (Watson *et al* 2004). In addition, we visually compared the reconstructed image and profile of an annulus phantom with the experimental image. The sinogram projections which included scatter obtained from a view of the direct sinogram were also compared. The phantom was a water-filled cylinder with both a length and diameter of 20 cm each, and included a smaller tube 20 cm in length with an outer diameter of 6 cm and inner diameter of 5 cm filled with ^{18}F solution located at a cylinder radius of 5 cm. The experimental image was acquired by an emission scan of 20 min with 185 MBq ^{18}F solution in the tube after a transmission of 20 min using three ^{68}Ga/^{68}Ge sources.

The simulation images were obtained using the following procedures. Two gamma rays (511 keV) with back-to-back angular distributions were radiated on the target phantom. In order to reduce computation time we did not simulate transportation of positrons. We took into account the following electromagnetic processes: Compton scatter, photoelectric effect, Rayleigh scatter, multiple scatter, bremsstrahlung, and ionization. The first three processes involve gamma rays, while the rest involve electrons. Positions where gamma rays interacted with the scintillator and deposited their energy were stored in (x, y, z) coordinates in the list mode. We did not blur the interacting points. The energy resolution was set to 15% (FWHM). The value was experimentally determined from energy spectra of the whole detector system by counting the number of single events for each energy window set to 195–205, 205–215, ... and 695–705 keV. We then created a 3D sinogram in the ECAT 3D format. Finally, we reconstructed the image into a 128 $\times$ 128 matrix and 47 slices by Fourier rebinning and filtered backprojection (FBP) with attenuation correction and scatter correction based on the single scatter simulation (Watson *et al* 1995, Ollinger 1996, Watson *et al* 1997). The image reconstruction including these corrections was performed by the PET software (ECAT 7.2: Siemens). The attenuation map was calculated analytically from the tissue data. The normalization was also performed analytically. In the normalization we did not correct for the fluctuation of detector gains because of the uniform gains in the simulation.

2.5. Simulation of a cardiac PET examination using ^{15}O-water

We investigated the effects of scatter on the simulation's quantification of MBF and PTF. We assigned activities to the myocardium, cardiac cavities, liver, and lung of the numerical human model and created 3D sinograms of each area. For each area 3 $\times$ 10^9 pairs of gamma rays were assessed. We then combined the sinograms at a ratio of organ activity that was estimated based on an experimental time activity curve (TAC) (Bq/mL) obtained from a clinical cardiac examination and the organ volumes (mL) of the numerical human model (myocardium: 410 mL; liver: 1161 mL; lung: 3341 mL; cardiac cavities: 480 mL) under the assumption that the activity of each organ was homogeneous. The clinical examination was performed with a patient (male, age 57 yr) using ECAT ACCEL and ^{15}O-water; images were reconstructed into 38 frames (5 s $\times$ 24, 15 s $\times$ 8, 30 s $\times$ 6) by FBP with attenuation and scatter corrections. The protocol was approved by the local ethics committee of the National Cerebral and Cardiovascular Center.

To construct the experimental TAC, regions of interest (ROIs) were carefully drawn at the centers of organs to avoid spillover. With respect to the myocardium, it is difficult to remove spillover so we estimated the TAC using the equation $C(t) = \mathrm{PTF} \cdot \mathrm{MBF} \cdot a(t) \otimes \exp(-\mathrm{MBF} \cdot t/p)$ for a conventional single-tissue compartment model (Kety 1951, 1960) assumed to have 1.0 mL/min/g of MBF and 1.0 g mL^{-1} of PTF ($C(t)$ = TAC of myocardium, $a(t)$ = experimental input function, $p = 0.91$ for water partition coefficient, and t = time). We converted the combined sinogram to the ECAT 3D format, and reconstructed the following

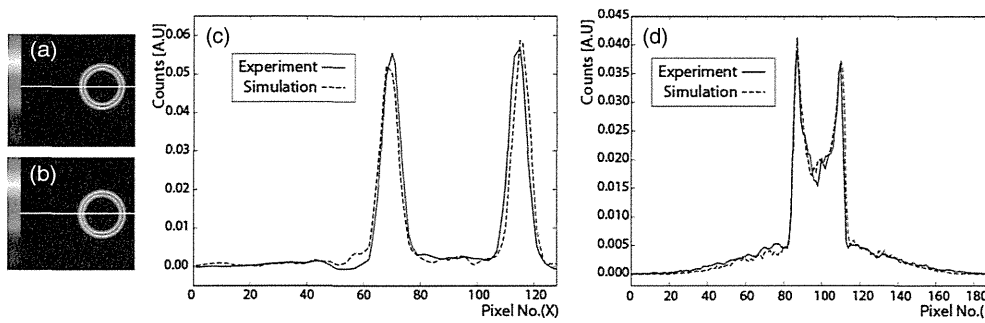

Figure 2. (a) and (b) show reconstruction images of the phantom of a simplified myocardium obtained from the experiment and the simulation, respectively. (c) Profiles at the levels of the white lines in (a) and (b), normalized by total counts. (d) Sinogram projections normalized by total counts obtained from the experiment and the simulation. These projections were taken from a view of the direct sinogram.

four image types using the FBP method without any smoothing filters: scatter-corrected image (SC), scatter-uncorrected image (W/O SC), attenuation-uncorrected image (W/O AC), and true image (TRUE). TRUE, which cannot be obtained experimentally, was reconstructed using a sinogram in which scatter was eliminated completely. For this type of image, scatter correction was not carried out, but correction was made for gamma ray attenuation. We compared SC with TRUE to evaluate the accuracy of the scatter correction implemented by the PET software. If the scatter correction was sufficiently accurate, SC would be equivalent to TRUE. We created 76 3D sinograms (38 frames for TRUE and 38 frames for SC, W/O AC and W/O SC) and reconstructed them into simulation images with different organ ratios (e.g., myocardium : liver : lung : ventricles = 1 : 0.4 : 4.5 : 3.1 at the 15th frame) according to the TAC in figure 3. The reconstructed images were scaled, where the ROI value of the cavity of the left ventricle (LV) in the SC at the 15th frame corresponded to that of the experimental value. Finally, we calculated regional MBFs and PTFs with a single-tissue compartment model, including spillover correction for the left and right ventricles (Iida *et al* 1992, Hermansen *et al* 1998, Katoh *et al* 2004), for the four types of images. MBFs and PTFs were represented in 17-segment polar maps together with polar maps normalized by the values of TRUE, called true MBF and true PTF, respectively. In this simulation, neither cardiac nor respiratory motion was generated. A motionless heart and minimized spillover from the myocardium allowed us to use a TAC with LV as the input function.

Three billion pairs of gamma rays were propagated in each organ. The simulation was performed in parallel using five personal computers with comparable specifications (Linux operating system installed on a 2.4 GHz Intel Core 2 Quad with 2 GB of memory) and twenty processors. These computations took about 60 h to complete.

3. Results

3.1. Scatter fractions and phantom images

In order to check the adequacy of the simulation, we compared the scatter fractions and images of an annulus phantom obtained in both the experiment and the simulation. The scatter fractions in the experiment and the simulation were 45.0% and 45.9%, respectively. These values also agreed with the value (46.5%) obtained in another study (Herzog *et al* 2004) using the NEMA NU2–2001 standard. Figures 2(a) and (b) show images of the annulus phantom

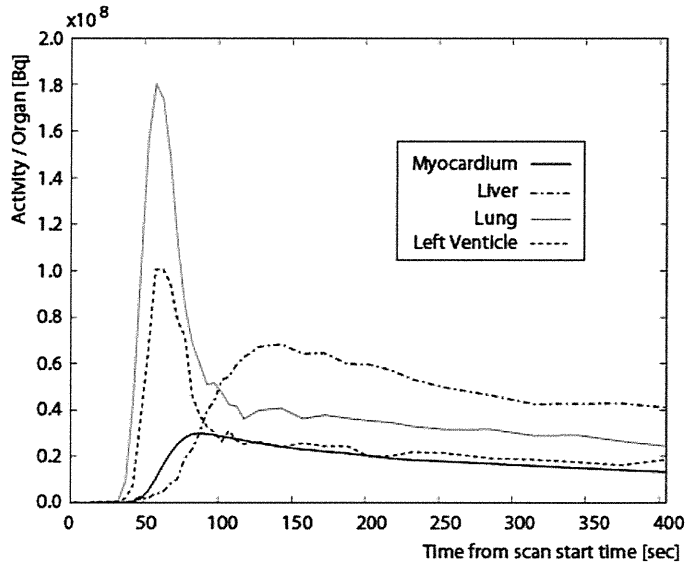

Figure 3. Activities in whole organs as functions of time. Activities were estimated from an experimental TAC (Bq/mL) and used organ volumes (mL) from the numerical human model (myocardium: 410 mL; liver: 1161 mL; lung: 3341 mL; cardiac pool: 480 mL).

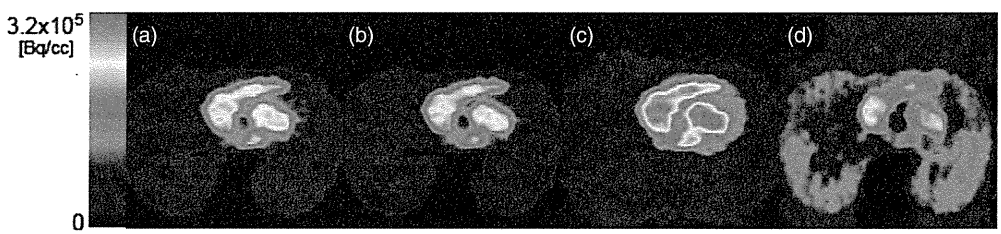

Figure 4. Representative simulation images at the center of the FOV (at the 15th frame). (a) Scatter-corrected image (SC). (b) True image (TRUE). (c) Scatter-uncorrected image (W/O SC). (d) Attenuation-uncorrected image (W/O AC) scaled by a factor of 10.

with activity in the tube from the experiment and the simulation, respectively. Figure 2(c) shows the profiles of the images at the levels of the white lines in figures 2(a) and (b), which were normalized by total counts. Figure 2(d) shows sinogram projections normalized by total counts obtained from the experiment and the simulation. The simulation image was visually consistent with the experimental image, and the profile had consistency. The ratio of peak to baseline counts in the simulation reproduced the experimental ratio within 6%. The simulation projection was also consistent with the experimental projections.

3.2. Quantification of MBF and PTF

The TAC (Bq) of each organ estimated from the clinical TAC (Bq/mL) and organ volumes (mL) of the numerical human model are shown in figure 3. Though the activity concentration of the lung was low, the activity of the whole lung was large due to its large volume, especially in the early phase. At 140 s from the scan start time, the portion of the liver adjacent to the heart had an activity approximately 2.5 times larger than that of the myocardium. Representative simulation images at the 15th frame (70 s from the scan start time) are shown in figure 4. TRUE

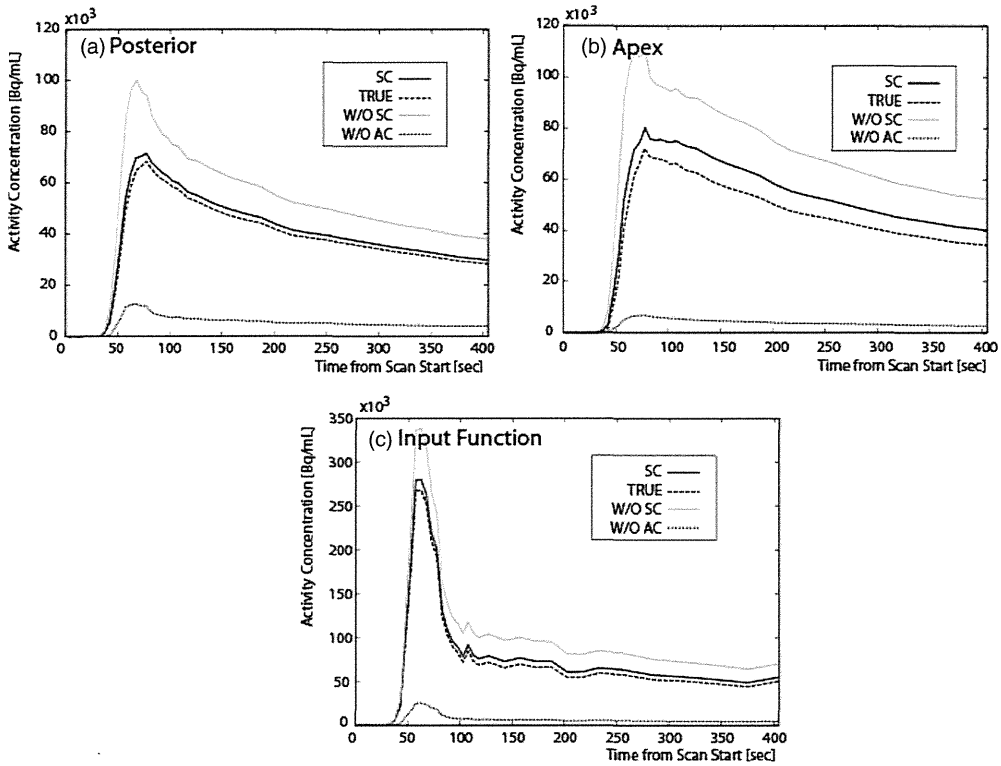

Figure 5. (a) TAC of posterior myocardium, (b) TAC of apex myocardium, (c) input function (TAC of left ventricle cavity obtained from the simulation for each type of image). Abbreviations; SC, TRUE, W/O SC and W/O AC stand for scatter-corrected image, true image, scatter-uncorrected image, and attenuation-uncorrected image, respectively.

was sharply defined because scatter was fully eliminated, while other images were relatively blurred. The SC image however was almost equivalent to TRUE image. An input function (TAC of the LV) and TAC of posterior and apex myocardium are shown in figure 5. The TAC derived from the SC corresponded to that derived from TRUE both in the input function and the posterior myocardium, and even higher activity existed in the portions of the liver and lung located partially outside the FOV. This tendency was observed for other areas of the myocardium except for the apex, for which the TAC was overestimated by approximately 15%. Polar maps of MBF calculated from dynamic simulation images are shown in figures 6(a)–(d), while normalized maps based on the true MBF are depicted in figures 6(e)–(g). Polar maps of PTF and the normalized maps are shown in figure 7. Means $\pm$ SD of normalized MBFs of SC, W/O AC, and W/O SC were 1.03 $\pm$ 0.05, 1.08 $\pm$ 0.18, and 1.13 $\pm$ 0.08, respectively. As for the normalized PTF, means of SC, W/O AC, and W/O SC were 1.00 $\pm$ 0.07, 1.35 $\pm$ 0.50 and 0.85 $\pm$ 0.09, respectively. Although equivalent MBFs within about 10% were obtained from all types of images, only the PTF of SC was close in value to the true PTF.

4. Discussion

4.1. Adequacy of the simulation

The scatter fraction obtained in the simulation was in good agreement with the experimental value. Scatter reproducibility is essential for our simulation in order to accurately estimate

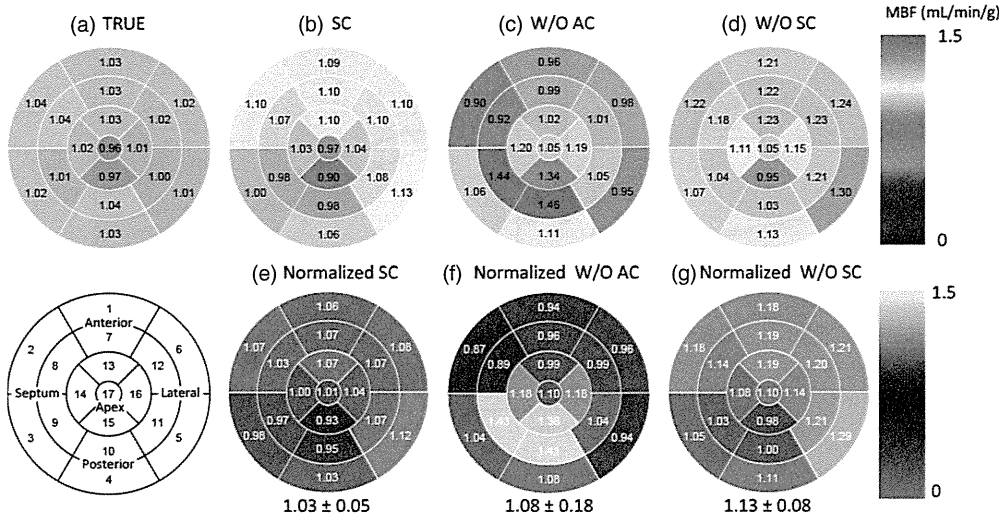

Figure 6. (a)–(d) Polar maps of absolute MBF. (e)–(g) Polar maps of MBFs normalized by the true MBF. The means ± SDs of normalized MBFs were 1.03 ± 0.05, 1.08 ± 0.18 and 1.13 ± 0.08 for SC, W/O AC, and W/O SC, respectively. Legend abbreviations are the same as in figure 5.

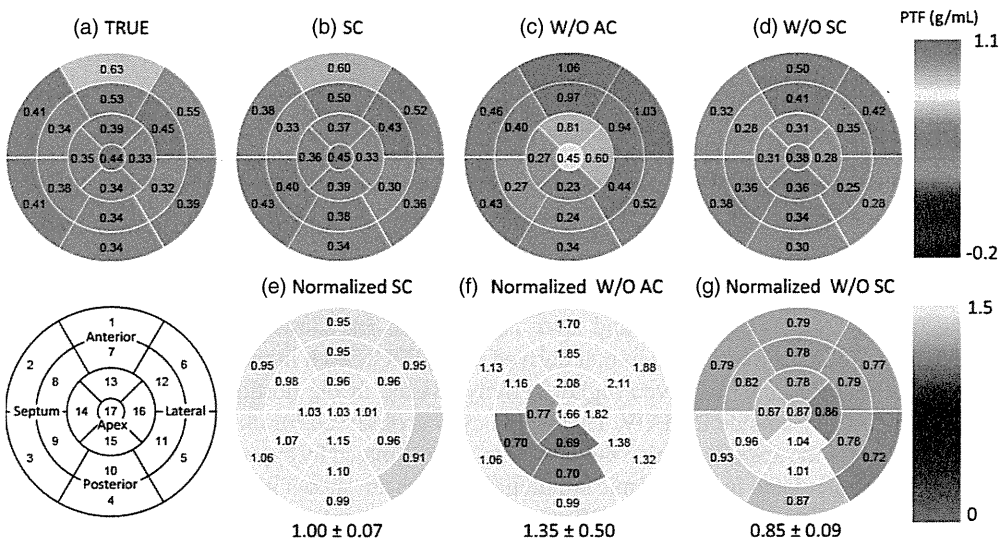

Figure 7. (a)–(d) Polar maps of absolute PTF. (e)–(g) Polar maps of PTF normalized by the true PTF. The means ± SDs of normalized PTFs were 1.00 ± 0.07, 1.35 ± 0.50 and 0.85 ± 0.09 for SC, W/O AC, and W/O SC, respectively. Legend abbreviations are the same as in figure 5.

the influence of scatter on quantitative MBF and PTF, the values of which this simulation determined with good accuracy. Furthermore, the simulation image of the phantom and profiles were also consistent with the experimental data. In these profiles, tails of peaks were small, which indicated that scatter was corrected accurately in both the simulation and the experiment. The sinogram projections also had consistency. Differing from the profiles of the images, scatter was still not corrected, resulting in tails of the peaks being observed.

The simulation is therefore appropriate in fulfilling the purpose of this study, and should be a reliable tool for estimation of scatter in 3D-PET.

4.2. Effects of scatter on MBF and PTF

TAC of the SC coincided with that of TRUE, indicating that scatter was accurately corrected. For the myocardial apex, the TAC of the SC was overestimated (15%) and was relatively larger than for other myocardium regions. This was likely due to uncorrected scatter originating from the liver bordered by the apex, because a similar simulation that excluded the activities of liver and lung demonstrated less overestimation. Absolute TAC without corrections naturally was much different from true TAC. The TAC of W/O AC was much smaller, because arms of the numerical human model beside the body caused strong absorption. However, absolute MBFs derived from not only SC but also W/O SC and W/O AC were in agreement with MBFs of TRUE regardless of the differences between absolute TAC. This is because MBF was calculated from the washout rate of the tracer, and the washout rates for all types of images were similar. This simulation showed that scatter and absorption did not change the shape of the TAC in the clearance phase. Our finding that MBFs derived from W/O AC and SC were equivalent was consistent with the results of Lubberink *et al* (2010), which were observed in a clinical context. However, in our simulation, MBF of the septum and posterior myocardium (segment numbers 9 and 10 of W/O AC in figure 6) was overestimated by about 40%. This was because spillover originated from lung activity, and the lung was located close to the myocardium in the numerical human model. In a similar simulation that did not include lung activity, the overestimation was reduced to almost zero. As this simulation has indicated, scatter and absorption have a small effect on the clearance rate of ^{15}O-water, and variation of absolute MBF of almost segment is suppressed within about 10% even without attenuation and scatter corrections. This is one of the advantages of ^{15}O-water in such scans.

In contrast to MBF, scatter correction is clearly essential for accurate PTF measurement. Although PTF derived from SC had good agreement with TRUE, PTF was overestimated by 35% for W/O AC and underestimated by 15% for W/O SC. For W/O SC, due to scatter effects we observed a relatively large overestimation in the input function rather than the tissue TAC $C(t)$, as shown in figure 5. This resulted in underestimation of the PTF value because PTF was roughly proportional to $C(t)/a(t)$. For W/O AC, regional dependencies of errors on PTF values were observed. From anterior to lateral regions (segment numbers 1, 6, 7, 12 and 13 of W/O AC), overestimation of PTF values was found because photon attenuation was smaller in the myocardial regions, $C(t)$, compared to the LV cavity, $a(t)$. From septal to posterior regions near the apex (segment numbers 9, 10, 14 and 15 of W/O AC), a significant attenuation effect in the myocardial regions rather than the LV cavity resulted in underestimation of PTF values.

PTF or perfusable tissue index (PTI) defined by PTF/ATF (anatomic tissue fraction) is useful as a marker of myocardial viability (Knaapen *et al* 2003), and several studies on the relationship between PTI and myocardial viability have been made (Yamamoto *et al* 1992, de Silva *et al* 1992, Gerber *et al* 1998, Itoh *et al* 2002). PTI can also be potentially used to noninvasively assess myocardial fibrosis (Knaapen *et al* 2004). Use of a ^{15}O-water scan sequential to a ^{15}O-CO scan could provide not only quantitative MBF but also PTI, which would also be the advantage of ^{15}O cardiac PET. The ^{15}O-CO scan, together with a transmission scan, is needed for calculation of ATF; however a single low-dose CT scan could provide ATF and serve as a substitute for these scans, resulting in reduction of scan duration, radiation dose, and risk of patient motion between scans (Harms *et al* 2011).

In the simulation, spillover was minimized because gamma ray detection points could be identified absolutely and the heart was motionless. Nevertheless, some spillover was still

observed due to the binning and interpolation involved in creating sinograms and image reconstruction, which caused about 0.3 of arterial blood volume. This simulation did not include other causes of spillover such as limited spatial resolution, positron range, cardiac motion, etc. However, even if these were included, current results would be considered valid because scatter distribution and the myocardium image would only be blurred.

The methodology developed in this work can be applied to other tracers to estimate the effects of scatter on absolute MBF. In addition, we can investigate the influence of positron range and cardiac motion on spillover and quantification of MBF. Geant4 enables propagation of positrons, and the XCAT phantom (Segars *et al* 2010) that provides the possibility of cardiac motion.

5. Conclusion

We investigated the effects of scatter on quantitative myocardium blood flow (MBF) and perfusable tissue fraction (PTF) using a precise three-dimensional positron emission tomography (3D-PET) simulation with a numerical human model. The simulation had good agreement with the experimental scatter fraction and a phantom image. In this simulation of a cardiac 3D-PET scan, scatter was corrected accurately for every region of the myocardium, and absolute MBFs remained unchanged even when the scatter and attenuation corrections were not applied. This simulation demonstrated that quantification of MBF using 3D-PET and ^{15}O-water was less affected by scatter and absorption. In contrast, to obtain accurate PTF, scatter correction was necessary.

Acknowledgments

This research was partially supported by a 2009 Grant-in-Aid for Young Scientists (B), no 21791237, from the Ministry of Education, Culture, Sports, Science and Technology of Japan.

References

Agostinelli S *et al* 2003 GEANT4 a simulation toolkit *Nucl. Instrum. Methods Phys. Res.* A **506** 250–303

Akkurt H and Echerman F K 2007 Development of PIMAL: mathematical phantom with moving arms and legs *Oak Ridge National Laboratory Report* ORNL/TM-2007/14

Brink I, Schumacher T, Talazko J, Reuland P, Mix M, Schindler T, Moser E A and Nitzsche E U 1991 3D-cardiac-PET: a recommendable clinical alternative to 2D-cardiac-PET? *Clin. Positron Imaging* **2** 191–6

Cherry S R, Woods R P, Hoffman E J and Mazziotta J C 1993 Improved detection of focal cerebral blood flow changes using three-dimensional positron emission tomography *J. Cereb. Blood Flow Metab.* **13** 630–8

deKemp R A, Yoshinaga K and Beanlands R S 2007 Will 3-dimensional PET-CT enable the routine quantification of myocardial blood flow? *J. Nucl. Cardiol.* **14** 380–97

de Silva R, Yamamoto Y, Rhodes C G, Iida H, Nihoyannopoulos P, Davies G J, Lammertsma A A, Jones T and Maseri A 1992 Preoperative prediction of the outcome of coronary revascularization using positron emission tomography *Circulation* **86** 1738–42

Gerber B L, Melin J A, Bol A, Labar D, Cogneau M, Michel C and Vanoverschelde J L 1998 Nitrogen-13-ammonia and oxygen-15-water estimates of absolute myocardial perfusion in left ventricular ischemic dysfunction *J. Nucl. Med.* **39** 1655–62

Harms H J, de Haan S, Knaapen P, Allaart C P, Lammertsma A A and Lubberink M 2011 Parametric images of myocardial viability using a single 15O-H2O PET/CT scan *J. Nucl. Med.* **52** 745–9

Hermansen F, Rosen S D, Fath-Ordoubadi F, Kooner J S, Clark J C, Camici P G and Lammertsma A A 1998 Measurement of myocardial blood flow with oxygen-15 labelled water: comparison of different administration protocols *Eur. J. Nucl. Med.* **25** 751–9

Herzog H, Tellmann L, Hocke C, Pietrzyk U, Casey M E and Kuwrt T 2004 NEMA NU2–2001 guided performance evaluation of four Siemens ECAT PET scanners *IEEE Trans. Nucl. Sci.* **51** 2662–9

Hirano Y, Koshino K and Iida H 2010 A Monte Carlo estimation of effects of activity outside field of view in O-15 cardiac 3D-PET *IEEE Med. Imaging Conf. Rec.* 2535–8

Ibaraki M, Miura S, Shimosegawa E, Sugawara S, Mizuta T, Ishikawa A and Amano M 2008 Quantification of cerebral blood flow and oxygen metabolism with 3-dimensional PET and 15O: validation by comparison with 2-dimensional PET *J. Nucl. Med.* **49** 50–9

Iida H, Rhodes C G, de Silva R, Araujo L I, Bloomfield P M, Lammertsma A A and Jones T 1992 Use of the left ventricular time-activity curve as a noninvasive input function in dynamic oxygen-15-water positron emission tomography *J. Nucl. Med.* **33** 1669–77 (available at http://jnm.snmjournals.org/content/33/9/1669.short)

Itoh H *et al* 2002 Perfusable tissue index obtained by positron emission tomography as a marker of myocardial viability in patients with ischemic ventricular dysfunction *Circ. J.* **66** 341–4

Katoh C, Morita K, Shiga T, Kubo N, Nakada K and Tamaki N 2004 Improvement of algorithm for quantification of regional myocardial blood flow using ^{15}O-water with PET *J. Nucl. Med.* **45** 1908–16 (available at http://jnm.snmjournals.org/content/45/11/1908.short)

Kety S S 1951 The theory and applications of exchange of inert gas at the lungs and tissues *Pharmacol. Rev.* **3** 1–41

Kety S S 1960 Measurement of local blood flow by the exchange of an inert diffusible substance *Methods Med. Res.* **8** 228–36

Knaapen P, Boellaard R, Götte M J, Dijkmans P A, van Campen L M, de Cock C C, Luurtsema G, Visser C A, Lammertsma A A and Visser F C 2004 Perfusable tissue index as a potential marker of fibrosis in patients with idiopathic dilated cardiomyopathy *J. Nucl. Med.* **45** 1299–304 (available at http://jnm.snmjournals.org/content/45/8/1299.short)

Knaapen P, Boellaard R, Götte M J, van der Weerdt A P, Visser C A, Lammertsma A A and Visser F C 2003 The perfusable tissue index: a marker of myocardial viability *J. Nucl. Cardiol.* **10** 684–91

Knaapen P *et al* 2010 Cardiac PET/CT: advanced hybrid imaging for the detection of coronary artery disease *Neth. Heart J.* **18** 90–8

Knesaurek K, Machac J, Krynyckyi B R and Almeida O D 2003 Comparison of 2-dimensional and 3-dimensional 82Rb myocardial perfusion PET imaging *J. Nucl. Med.* **44** 1350–6 (available at http://jnm.snmjournals.org/content/44/8/1350.short)

Knuuti J, Kajander S, Mäki M and Ukkonen H 2009 Quantification of myocardial blood flow will reform the detection of CAD *J. Nucl. Cardiol.* **6** 497–506

Lodge M A, Badawi R D, Gilbert R, Dibos P E and Line B R 2006 Comparison of 2-dimensional and 3-dimensional acquisition for 18F-FDG PET oncology studies performed on an LSO-based scanner *J. Nucl. Med.* **47** 23–31 (available at http://jnm.snmjournals.org/content/47/1/23.short)

Lubberink M, Boellaard R, van der Weerdt A P, Visser F C and Lammertsma A A 2004 Quantitative comparison of analytic and iterative reconstruction methods in 2- and 3-dimensional dynamic cardiac 18F-FDG PET *J. Nucl. Med.* **45** 2008–15 (available at http://jnm.snmjournals.org/content/45/12/2008.short)

Lubberink M, Harms H J, Halbmeijer R, de Haan S, Knaapen P and Lammertsma A A 2010 Low-dose quantitative myocardial blood flow imaging using 15O-water and PET without attenuation correction *J. Nucl. Med.* **51** 575–80

Moreno-Cantu J J, Thompson C J and Zatorre R J 1998 Evaluation of the ECAT EXACT HR1 3-D PET scanner in H2O-15 brain activation studies: dose fractionation strategies for rCBF and signal enhancing protocols *IEEE Trans. Med. Imaging* **17** 979–85

Nagaoka T, Watanabe S, Sakurai K, Kunieda E, Watanabe S, Taki M and Yamanaka Y 2004 Development of realistic high-resolution whole-body voxel models of Japanese adult male and female of average height and weight, and application of models to radio-frequency electromagnetic-field dosmietry *Phys. Med. Biol.* **49** 1–15

Ollinger J M 1996 Model-based scatter correction for fully 3D PET *Phys. Med. Biol.* **41** 153–176

Roelants V, Bol A, Bernard X, Coppens A, Melin J, Gerber B and Vanoverschelde J L 2006 Direct comparison between 2-dimensional and 3-dimensional PET acquisition modes for myocardial blood flow absolute quantification with O-15 water and N-13 ammonia *J. Nucl. Cardiol.* **13** 220–4 (available at http://www.onlinejnc.com/journal/12350/13/2/BF02971246_10.1007_BF02971246/2008/Direct_comparison_between_2-dimensional_and_3-dime.html)

Sadato N, Carson R E, Daube-Witherspoon M E, Campbell G, Hallett M and Herscovitch P 1997 Optimization of noninvasive activation studies with 15O-water and three-dimensional positron emission tomography *J. Cereb. Blood Flow Metab.* **17** 732–9

Schäfers K P, Spinks T J, Camici P G, Bloomfield P M, Rhodes C G, Law M P, Baker C S and Rimoldi O 2002 Absolute quantification of myocardial blood flow with H2 15O and 3-dimensional PET: an experimental validation *J. Nucl. Med.* **43** 1031–40 (available at http://jnm.snmjournals.org/content/43/8/1031.short)

Schepis T, Gaemperli O, Treyer V, Valenta I, Burger C, Koepfli P, Namdar M, Adachi I, Alkadhi H and Kaufmann P A 2007 Absolute quantification of myocardial blood flow with 13N-ammonia and 3-dimensional PET *J. Nucl. Med.* **48** 1783–9

Segars W P, Sturgeon G, Mendonca S, Grimes J and Tsui B M 2010 4D XCAT phantom for multimodality imaging research *Med. Phys.* **37** 4902–15

Votaw J R and White M 2001 Comparison of 2-dimensional and 3-dimensional cardiac ^{82}Rb PET studies *J. Nucl. Med.* **42** 701–6 (available at http://jnm.snmjournals.org/content/42/5/701.short)

Watson C C, Casey M E, Eriksson L, Mulnix T, Adams D and Bendriem B 2004 NEMA NU 2 performance tests for scanners with intrinsic radioactivity *J. Nucl. Med.* **45** 822–6 (available at http://jnm.snmjournals.org/content/45/5/822.short)

Watson C C, Newport D and Casey M E 1995 A single scatter simulation technique for scatter correction in 3D PET *Proc. Int. Meeting on Fully Three-Dimensional Image Reconstruction in Radiology and Nuclear Medicine* pp 215–9

Watson C C, Newport D, Casey M E, deKemp R A, Beanlands R S and Schmand M 1997 Evaluation of simulation-based scatter correction for 3-D PET cardiac imaging *IEEE Trans. Nucl. Sci.* **44** 90–97

Yamamoto Y *et al* 1992 A new strategy for the assessment of viable myocardium and regional myocardial blood flow using ^{15}O-water and dynamic positron emission tomography *Circulation* **86** 167–78

IOP PUBLISHING PHYSICS IN MEDICINE AND BIOLOGY

Phys. Med. Biol. **57** (2012) 7873–7892 doi:10.1088/0031-9155/57/23/7873

Quantitative assessment of regional cerebral blood flow by dynamic susceptibility contrast-enhanced MRI, without the need for arterial blood signals

Jun-ichiro Enmi[1], Nobuyuki Kudomi[2], Takuya Hayashi[3], Akihide Yamamoto[1], Satoshi Iguchi[1], Tetsuaki Moriguchi[1], Yuki Hori[1], Kazuhiro Koshino[1], Tsutomu Zeniya[1], Nadim Jon Shah[4,5], Naoaki Yamada[6] and Hidehiro Iida[1]

[1] Department of Investigative Radiology, National Cerebral and Cardiovascular Center Research Institute, 5-7-1 Fujishiro-dai, Suita City, Osaka 565-8565, Japan
[2] Department of Medical Physics, Faculty of Medicine, Kagawa University, Ikenobe 1750-1, Miki-cho, Kita-gun, Kagawa, 761-0793, Japan
[3] Functional Probe Research Laboratory, RIKEN Center for Molecular Imaging Science, 6-7-3 Minatojima-minamimachi, Chuo-ku, Kobe, Hyogo, 650-0047, Japan
[4] Institute of Neuroscience and Medicine-4, Medical Imaging Physics, Forschungszentrum Jülich GmbH, 52425 Jülich, Germany
[5] Department of Neurology, Faculty of Medicine, JARA, RWTH Aachen University, 52074 Aachen, Germany
[6] Department of Radiology, National Cerebral and Cardiovascular Center, 5-7-1 Fujishiro-dai, Suita City, Osaka 565-8565, Japan

E-mail: enmi.junichiro.ri@mail.ncvc.go.jp

Received 18 December 2011, in final form 2 September 2012
Published 14 November 2012
Online at stacks.iop.org/PMB/57/7873

Abstract

In dynamic susceptibility contrast-enhanced magnetic resonance imaging (DSC-MRI), an arterial input function (AIF) is usually obtained from a time–concentration curve (TCC) of the cerebral artery. This study was aimed at developing an alternative technique for reconstructing AIF from TCCs of multiple brain regions. AIF was formulated by a multi-exponential function using four parameters, and the parameters were determined so that the AIF curves convolved with a model of tissue response reproduced the measured TCCs for 20 regions. Systematic simulations were performed to evaluate the effects of possible error sources. DSC-MRI and positron emission tomography (PET) studies were performed on 14 patients with major cerebral artery occlusion. Cerebral blood flow (CBF) images were calculated from DSC-MRI data, using our novel method alongside conventional AIF estimations, and compared with those from ^{15}O-PET. Simulations showed that the calculated CBF values were sensitive to variations in the assumptions regarding cerebral blood volume. Nevertheless, AIFs were reasonably reconstructed for all patients. The difference in CBF values between DSC-MRI and PET was -2.2 ± 7.4 ml/100 g/min ($r = 0.55$, $p < 0.01$) for our method, versus -0.2 ± 8.2 ml/100 g/min ($r = 0.47$, $p = 0.01$) for the conventional method.

0031-9155/12/237873+20$33.00 Printed in the UK & the USA 7873

The difference in the ratio of affected to unaffected hemispheres between DSC-MRI and PET was 0.07 ± 0.09 ($r = 0.82$, $p < 0.01$) for our method, versus 0.07 ± 0.09 ($r = 0.83$, $p < 0.01$) for the conventional method. The contrasts in CBF images from our method were the same as those from the conventional method. These findings suggest the feasibility of assessing CBF without arterial blood signals.

(Some figures may appear in colour only in the online journal)

1. Introduction

Quantitation of cerebral blood flow (CBF) provides essential information about pathophysiological status in cerebral ischemic disease. Dynamic susceptibility contrast-enhanced magnetic resonance imaging (DSC-MRI) has been extensively utilized to assess quantitative or semi-quantitative CBF images in clinical settings (Calamante *et al* 1999). The most commonly accepted technique for quantitation is based on the deconvolution of the time–concentration curve (TCC) of cerebral tissues using the arterial input function (AIF), as originally proposed by Østergaard and co-workers (Østergaard *et al* 1996a, 1996b).

In general, AIF is required in quantitative assessment of perfusion in cerebral and other tissue. In the field of nuclear medicine, the standard technique for obtaining AIF is based on the arterial blood sampling. The arterial-blood-sampling-based technique has also been applied to quantitative assessment of perfusion using MRI with gadopentetate dimeglumine (Gd-DTPA) (Larsson *et al* 1990, Fritz-Hansen *et al* 1996), but is invasive and requires labor intensive works. Thus, AIF has normally been obtained from the arterial blood signals obtained from MR images by selecting regions of interest (ROIs) on a pertinent artery, e.g., the internal carotid artery (ICA), middle cerebral artery (MCA) (Calamante *et al* 1999), or aorta (Brix *et al* 2004). Such a technique (the arterial voxel selection method) however suffers from errors attributed to the cross contamination between the artery and adjacent tissue or the partial volume effect (van Osch *et al* 2001, Hansen *et al* 2009). It is also important to note that the nonlinear relationship exists between the tracer concentration and the relaxation rate (van Osch *et al* 2003), causing systematic errors in AIF thus in CBF.

Recently, an alternative technique has been developed by Yang *et al* (2004, 2007) and Schabel *et al* (2010a, 2010b), with the intention of reducing the effects to the partial volume effect, and minimizing errors caused by the nonlinear relationship between contrast agent concentrations and relaxation time. In such techniques, AIF was reconstructed from tissue TCCs; thus errors attributed to the partial volume effect could be reduced. An additional advantage of this approach is the reduced dynamic range of MR signals. Recently, our group proposed a technique to reconstruct AIF from tissue time–activity curves (TTACs) in PET, based on a mathematical formulation that describes the AIF with only a small number of parameters (Kudomi *et al* 2008). The parameters were determined so that TTACs in multiple tissue regions simulated by the convolution of the AIF by tissue-response functions reproduced the observed TTAC best by means of the nonlinear least-squares minimization procedures. This study demonstrated that the AIF could be accurately reproduced from a sequential PET image obtained with i.v. ^{15}O-water, enabling the quantitative assessment of regional hepatic blood flow images in clinical settings.

In this study, we extended the tissue-based method of Kudomi *et al* (2008) to the quantitatively assessment of CBF in the DSC-MRI. Verification of this method was first evaluated by systematic simulations, and then validated in patient population, by referring the PET technique as a gold standard.

2. Materials and methods

2.1. Theory

To reconstruct AIF from TCCs of multiple brain regions, a model function was assumed for AIF:

$$C_{\mathrm{Artery}}(t) = \begin{cases} 0 & (t < t_1) \\ \frac{A}{K_e^2(1+\alpha)^2}[1 - \exp\{K_e(1+\alpha)(t_1 - t)\}] & (t_1 \leqslant t \leqslant t_2) \\ \frac{A}{K_e^2(1+\alpha)^2}[\exp\{K_e(1+\alpha)(t_1 - t_2)\} + \exp\{K_e(1+\alpha)(\mathrm{t}_2 - \mathrm{t})\} \\ \quad -2 \cdot \exp\{K_e(1+\alpha)(t_1 - t)\}] & (t > t_2) \end{cases} \quad (1)$$

where the model function was derived by assuming that the contrast agent is intravenously administered between t_1 and t_2 at a constant rate of A, and that the agent diffuses back and forth between arterial blood and whole-body interstitial spaces at rates αK_e and K_e, respectively (Kudomi *et al* 2008) (see figure 1(a)). The TCC of cerebral tissue ($C_{\mathrm{Tissue}}(t)$) in a given volume segment was expressed as

$$C_{\mathrm{Tissue}}(t) = f \cdot C_{\mathrm{Artery}}(t) \otimes \mathrm{e}^{-\frac{f}{v}t}, \quad (2)$$

where f and v are CBF and cerebral blood volume (CBV) in the volume segment, respectively. The residue function was assumed to follow a single-compartment model that could be expressed by a single-exponential function, consistent with an approach frequently used in previous simulation studies (Calamante *et al* 2000, 2007, Wu *et al* 2003a, Smith *et al* 2004, Salluzzi *et al* 2005, Willats *et al* 2006). TCCs of tissues were obtained from different brain regions of normal gray matter, and used in the AIF reconstruction as follows, as previously described (Kudomi *et al* 2008).

In addition to f for each region, four parameters describing the shape of the AIF (A, $K_e(1+\alpha)$, t_1 and t_2-t_1) were determined by means of the combination of nonlinear least-squares and grid search minimization, such that the TCCs of multiple brain regions were best fit to (2), as illustrated in figure 1(b). Detailed procedures are essentially the same as in the previous report (Kudomi *et al* 2008). Three important assumptions were made as follows. (1) There is a single AIF common over all brain regions, and therefore one set of the four parameters can be shared among all the tissues selected for reconstructing AIF; (2) while f varies among regions, CBV is assumed to have a constant value of 4 ml/100 g, a typical value for a normal gray-matter region (Yamaguchi *et al* 1986, Ito *et al* 2004); and (3) there is no difference in the tracer arrival time among different tissue regions. The second assumption is intended to provide a unique absolute scale (A), which corresponds to the height of AIF. If this assumption is absent, then only relative A, and hence relative f, can be determined. The AIF was computed by substituting the obtained parameter values into (1). CBF images were calculated by deconvolving the TCC of each voxel in dynamic MRI images with the reconstructed AIF.

2.2. Simulation study

Systematic simulations were carried out in order to evaluate the effects of possible errors on the reconstructed AIFs and resultant CBF values. The first simulation was carried out in order to evaluate the effect of the estimation error of each parameter describing the shape of the model function on resultant CBF value. In the second simulation, the effect of finite sampling period on the shape of reconstructed AIF and resultant CBF was evaluated. The third simulation was

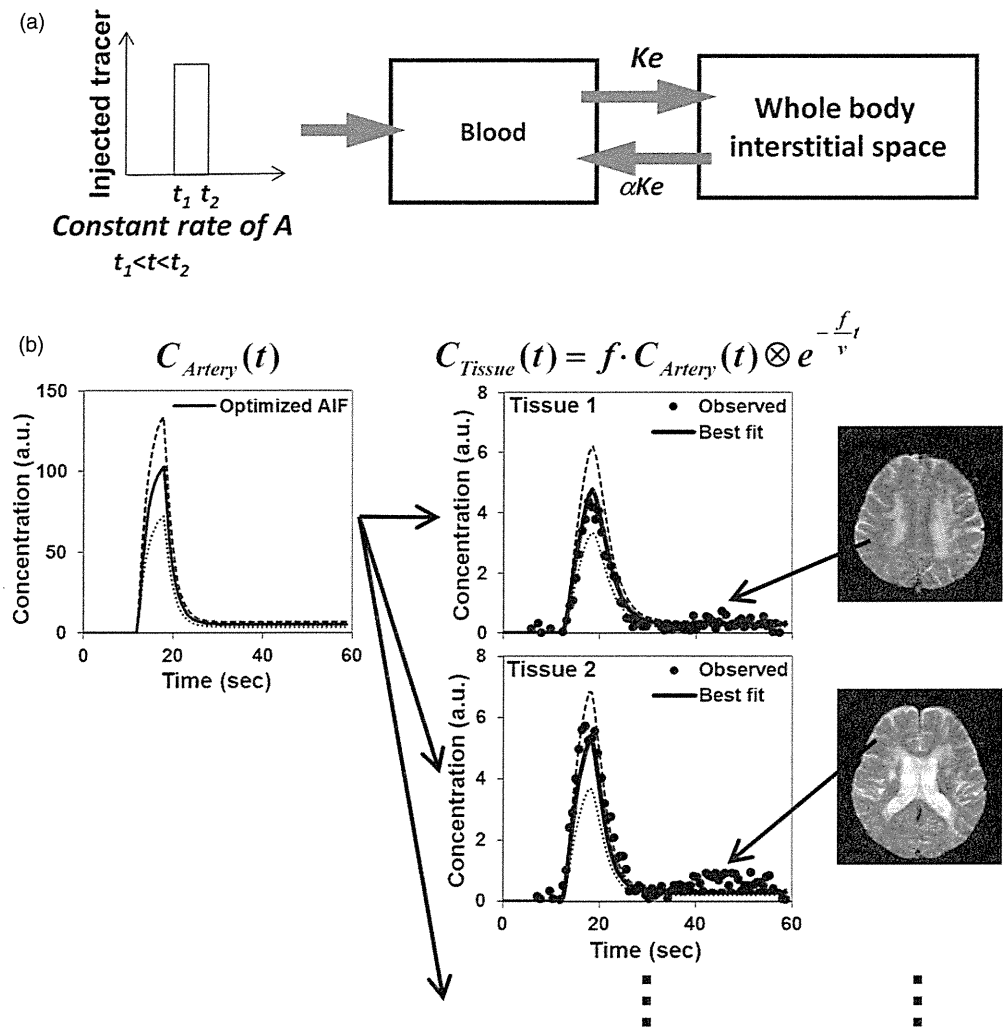

Figure 1. Procedures of reconstructing the arterial input function proposed in this paper. (a) Compartment model for creating the arterial input function (AIF). Four sets of parameters were defined to formulate the arterial input function. (b) The procedure for reconstructing an AIF from multiple tissue curves. The observed tissue curves are fitted to the theoretical tissue curves ($C_{tissue}(t)$) generated from the AIF model function ($C_{Artery}(t)$), which contains four unknown parameters (A, $K_e(1+\alpha)$, t_1 and t_2-t_1). The parameter values minimizing the sum of squared residuals for all tissue curves are selected as the optimal ones. The value of f is optimized for each region selected for AIF estimation. The AIF was obtained by substituting the optimized parameter values into equation (1).

intended to evaluate the error attributed to assumption 2, namely, how the discrepancy between actual and assumed CBV values affects the shape of the reconstructed AIF and resultant CBF value. The fourth simulation was intended to evaluate the error due to assumption 3, namely, how the variation of tracer appearance times among tissues selected for AIF reconstruction affects the shape of the reconstructed AIF and resultant CBF value. The fifth simulation was carried out to evaluate effects of statistical noise in the MR signals on calculated CBF values.

In these simulations, the AIF observed in one patient study was used as the true AIF. Using (2) and the true AIF, two TCCs were generated by assuming $f = 60$ ml/100 g/min, $v = 4$ ml/100 g, and $f = 30$ ml/100 g/min, $v = 4$ ml/100 g, corresponding to the respective values for normal and ischemic gray matter. In each simulation described below, CBF values of the two simulated tissues were calculated by deconvolution of the two TCCs with deliberately generated erroneous AIFs. The deconvolution procedure was the same as that described in section 2.3.2. The magnitude of errors in the calculated CBF values was then evaluated as a function of each error source. The sampling period was assumed to be 0.66 s, as in the present patient study. All TCCs of tissues in the simulations were generated using (2) and the true AIF.

In the first simulation, AIFs were generated using (1) by changing each of the model parameters (A, $K_e(1+\alpha)$ and t_2-t_1) from the true value to $\pm$ standard deviation (SD) (where the true values are the ones in the true AIF) and SDs were calculated over the total 14 patient studies. The value of t_1 was fixed at 12.2 s. While two out of A, $K_e(1+\alpha)$ and t_2-t_1 were fixed at true values, the other parameter was varied within the range of the true value $\pm$ SD.

In the second simulation, 20 TCCs of tissues were generated for each of the four different sampling periods (0.1, 0.5, 1.0 and 2.0 s). For all TCCs, the v value was assumed at 4 ml/100 g, while f values were randomly generated by assuming a Gaussian distribution with a mean of 60 ml/100 g/min and a SD of 12 ml/100 g/min (Calamante *et al* 2000, Yamaguchi *et al* 1986, Hatazawa *et al* 1995, Iida *et al* 1998, Ito *et al* 2000, 2002). For each sampling period, AIF was reconstructed from the 20 TCCs generated. In this and subsequent simulations, one set of 20 f values was shared.

In the third simulation, for values of v ranging from 3.5 to 4.5 ml/100 g in 0.1 ml/100 g steps, 20 TCCs of tissues were generated using randomly generated f values as described in the previous simulation; for each v value, AIF was reconstructed from the 20 TCCs generated. The examined range of CBV was determined based on the previously reported CBV values for normal gray matter (Yamaguchi *et al* 1986, Ito *et al* 2004).

In the fourth simulation, 20 TCCs of tissues were generated using randomly generated f values and a v value of 4 ml/100 g. The true AIF was utilized for generating the TCCs, but only the t_1 value was deliberately changed: t_1 was set at 12.2 s for 6 of the 20 TCCs, $12.2 + \Delta t/2$ s for other 7 TCCs, and $12.2 - \Delta t/2$ s for the rest. Twenty TCCs were randomly assigned to each of the three groups. For each value of Δt ranging from 0.0 to 4.0 s in 0.4 s steps, AIF was reconstructed from the 20 TCCs generated. The Δt of 4.0 s simulated the situation that the ROIs for AIF reconstruction are placed over a wide region ranging from top to base of the cerebrum.

In the fifth simulation, 20 TCCs of tissues were generated by assuming 20 CBF values employed in the second simulation. For all TCCs, the v value was assumed at 4 ml/100 g. Statistical noise of Gaussian distribution was added to these TCCs with the coefficient of variation (COV) of 1%, 2%, 4%, 6% and 8% to generate 50 sets of 20 TCCs for each noise level, as in previous reports (Henkelman 1985, Wu *et al* 2003b). An additional TCC was generated using the given AIF for $f = 60$ ml/100 g/min and $v = 4$ ml/100 g, from which 50 CBF values were calculated using each of 50 AIFs obtained from each of 50 sets of 20 TCCs as described in the theory. Mean and COV of the calculated CBF were then shown as a function of the noise level.

2.3. Patient study

2.3.1. Subjects. We retrospectively reviewed 14 patients (64 $\pm$ 12 years old; 11 males and 3 females) with chronic cerebral arterial occlusive disease in the ICA or MCA. Patients had